Imperial College London
Department of Physics

Investigating Detector Specifications for Ionacoustic Imaging of Proton Beams

Anthea E. MacIntosh-LaRocque

Student's CID: 01507986
Supervisor: Prof. Kenneth Long
Assessor: Dr. Jaroslaw Pasternak
Word count: 5834

Submitted for the FHEQ Level 6 module PHYS60016 - Year 3 Project 2021-2022 in the Department of Physics at Imperial College London. January - May 2022

CCAP-TN-INST-05

Abstract

Ionacoustics is an emerging dose mapping technique for proton beam therapy. This work presents a simulation of pressure waves emitted due to the stopping of a 200MeV proton beam in a water phantom and the subsequent detection of these waves with a hemispherical detector. The initial pressure distribution is reconstructed using an iterative time-reversal algorithm. The results of varying the detector diameter, z-position and the number of iterations in the reconstruction algorithm are presented and discussed. It is found that the detected frequency content varies significantly with the geometry of the detector. The work suggests the next steps required to improve the simulation, and ultimately identify a suitable detector configuration and reconstruction algorithm for a prototype of the detector which will eventually be used at the proposed LhARA facility.

Declaration of work undertaken

This was an individual project carried out between January and May 2022. I previously worked with the Centre for the Clinical Application of Particles (CCAP) at Imperial during a UROP in the summer of 2021. This work focuses on an area of research (ionoacoustic dose mapping) similar to what I studied during my UROP. However, this work focuses on the acoustic propagation of pressure and image reconstruction, which was entirely new to me when beginning this project.

In this project, I am responsible for:

- Collating and reading the literature cited in this report;
- Creating the code for modelling a sensor and reconstructing the initial pressure distribution;
- Analysing the simulation results and drawing conclusions.

Acknowledgements

I would like to thank my supervisor, Ken for his support throughout this project. Thank you to the LhARA Ionacoustic Work Package team for welcoming me into the group and providing insight into k-Wave and ionacoustics. Thank you to H.T. Lau for your help with the SmartPhantom side of the project.

Contents

1 Introduction

Proton beam therapy (PBT) is a form of radiotherapy used to target and kill tumour cells. Proton beams benefit from the ability to deposit a large amount of energy in a small volume, in comparison to the more conventional electron and photon beams, as shown in Fig. 1.

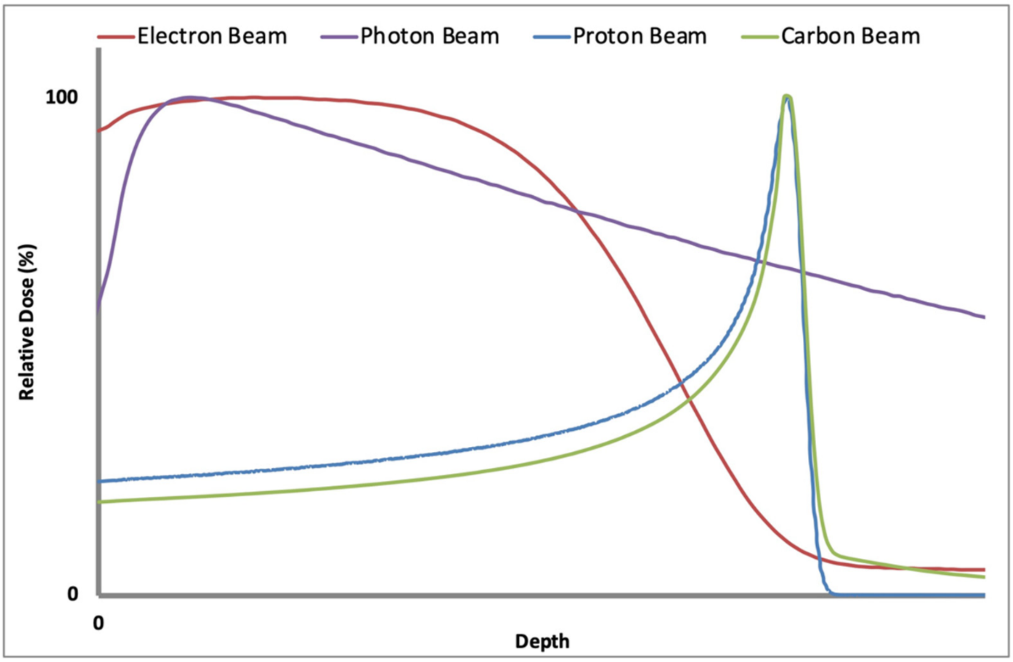

Figure 1: The relative dose-depth profiles of electrons (red curve), photons (purple curve), protons (blue curve), and carbon ions (green curve). Both the proton and carbon ion beams have distinct Bragg peaks. Unlike protons, the carbon ion curve features residual dose distribution downstream of the Bragg peak, due to fragmentation of the ion. The carbon Bragg peak is also sharper than that of the proton beam. The photon and electron beams deposit significant amounts of their energies at low depths. The electron beam has a relatively short penetration depth. The photon beam, on the other hand, deposits a high relative dose at large depths. Image from [1].

At present, the underlying biological processes by which protons interact with healthy tissue and tumours are not well understood. The Laser-hybrid Accelerator for Radiobiological Applications (LhARA) is a proposed facility to study PBT in order to better understand this radiotherapy technique. For this purpose it is critical to be able to provide accurate and precise online mapping of dose deposition in the target. LhARA envisages a mixture of scintillating fibre detectors and ionacoustic imaging to achieve this aim. For the initial prototype of this detector, a water phantom fitted with planes of scintillating fibre detectors in tandem with an on-axis hemispherical ionoacoustic detector will be constructed. Eventually this will be extended to provide dose mapping within irradiated biological samples suspended in the phantom. Ionacoustic imaging is in its beginning stages as a tool for proton beam dose mapping. A typical experimental set-up for an ionacoustic dose mapping is shown in Fig. 2.

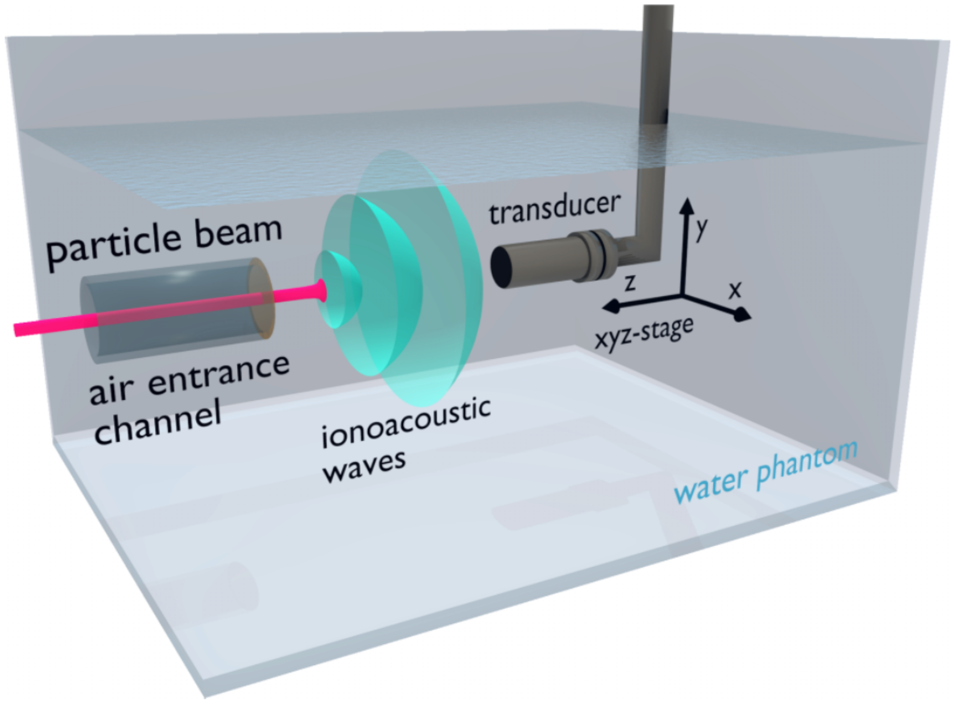

Figure 2: Visualisation of a typical ionacoustic experimental set-up. Image from [2].

Before beginning the construction of this prototype, it is imperative to validate the performance of the proposed detectors in mapping the dose distribution. This project uses acoustic simulations to emulate the reconstruction of the dose profile of a simulated test proton beam. Moreover, by varying the detector geometry (diameter d, z-position z_d) and number of iterations N used in the reconstruction algorithm, the effect of these parameters on the detector's performance is investigated. Finally, suggestions are made for the future work required to determine the ideal detector configuration and reconstruction algorithm.

1.1 Aims and Objectives

The primary objective of this project is to determine whether an ionoacoustic detector can be used to characterise the energy deposition of a proton beam in a water phantom using simulation. This overarching aim is supported by the following subsidiary objectives:

- Simulate dose deposition in a water phantom using Geant4 [3] and fit this deposition with the analytical distribution given in Bortfeld, 1997 [4];
- Characterise the required bandwidth and geometry of the detector for a test beam;
- Simulate the propagation of acoustic waves due to proton energy deposition to a detector using the MATLAB-based software k-Wave [5] [6];
- Reconstruct the initial pressure distribution using time reversal reconstruction based on the signal at the detector;
- Parameterise the inital and reconstructed pressure distributions with the analytical equation for dose deposition given in Bortfeld, 1997 [4];
- Determine to what degree the initial pressure distribution can be reconstructed using iterative time-reversal.

2 Background

2.1 Interactions between protons and matter

There are four mechanisms by which protons can interact with matter: inelastic Coulomb interactions with atomic electrons, elastic Coulomb interactions with atomic nuclei, non-elastic nuclear reactions with atomic nuclei and Bremsstrahlung [7]. Inelastic Coulomb interactions with atomic electrons are the primary source of energy loss for therapeutic proton beams. A proton will experience an elastic repulsive Coulomb force when passing close to an atomic nucleus, scattering the proton from its initial straight-line trajectory. Protons can react with the nuclei of atoms in non-elastic processes producing secondary particles including neutrons, heavy ions and secondary protons. Bremsstrahlung interactions result in negligible energy loss for protons at therapeutically relevant proton beam energies.

2.2 Proton beam therapy

One in five individuals will develop cancer in their lifetime, and one in ten will die from the disease. In 2020 alone, an estimated 19.3 million people were diagnosed with cancer and approximately 10.0 million deaths were attributed to cancer globally [8]. Radiotherapy, alongside chemotherapy and surgery, is one of the most widely used cancer treatments available today [9]. Radiotherapy is usually delivered by targeting tumour cells with photon or electron beams. In most cases, the radiation source comes from outside the patient, although some treatments involve a radiation source inserted within the tumour. When administered correctly, the interactions between matter and the photons or electrons elicit strand breaks in the DNA of the tumour cells. The primary challenge in radiotherapy is minimising damage to healthy tissue [10]. The dose-depth curves for photons and electrons in Fig. 1 illustrate the challenge this poses, particularly when the tumour is located far from the surface of the tissue: a large proportion of the radiation dose is deposited in the healthy tissue before reaching the targeted tumour [10].

PBT is an alternative radiotherapy technique first recognised in the 1940s. PBT remained experimental until 1990, when it became available as treatment in hospital-settings. Now, over 100 000 patients have been treated using PBT [11]. PBT presents a solution to minimising the damage to healthy tissue during radiotherapy, reducing adverse effects from treatment [12]. There are numerous experimental studies which support the effectiveness of PBT in treating cancer [13]. There is also active research into the use of enhanced technologies such as proton-minibeams to improve treatment outcomes [14] [15] [16] [17]. However, there is need for further research into this form of radiotherapy in order for it to become a widely accepted and utilised form of cancer treatment [18].

The physical mechanism by which PBT achieves such spatially localised energy deposition is as follows. The energy transferred during the electromagnetic interactions between protons and matter is inversely proportional to the velocity of the proton. As a result, as the protons slow down, the energy absorbed in tissue per unit length, known as the linear energy transfer (LET) increases. The electromagnetic interactions are primarily due to the proton interacting with electrons in matter. Moreover, as protons run out of energy and are stopped, the flux of protons in the tissue decreases. A decreased number of protons means that there are fewer statistical variations in proton range, resulting in a sharper peak [11]. This characteristic dose distribution peak is denoted the Bragg peak.

Bortfeld, 1997 [4] provides this analytical approximation of the Bragg curve, valid for beam energies between 10 and 200 MeV,

$$D(z) = \Phi_0 \frac{e^{-\xi^2/4}\sigma^{1/p}\,\Gamma(1/p)}{\sqrt{2\pi}\rho p \alpha^{1/p}(1+\beta R_0)} \left[\frac{1}{\sigma}\mathscr{D}_{-1/p}(-\xi) + \left(\frac{\beta}{p} + \gamma\beta + \frac{\epsilon}{R_0}\right)\mathscr{D}_{-1/p-1}(-\xi)\right], \qquad (1)$$

with parameters and constants defined in Table 1. An example of a Bragg curve for a 200 MeV proton beam is shown in Fig. 3.

While not discussed here, other heavy charged particles such as carbon and oxygen ions have the potential to be used in radiotherapy. Due to their higher mass, heavy-ions experience less scattering, resulting in a sharper Bragg peak. However, nuclear interaction between the heavy

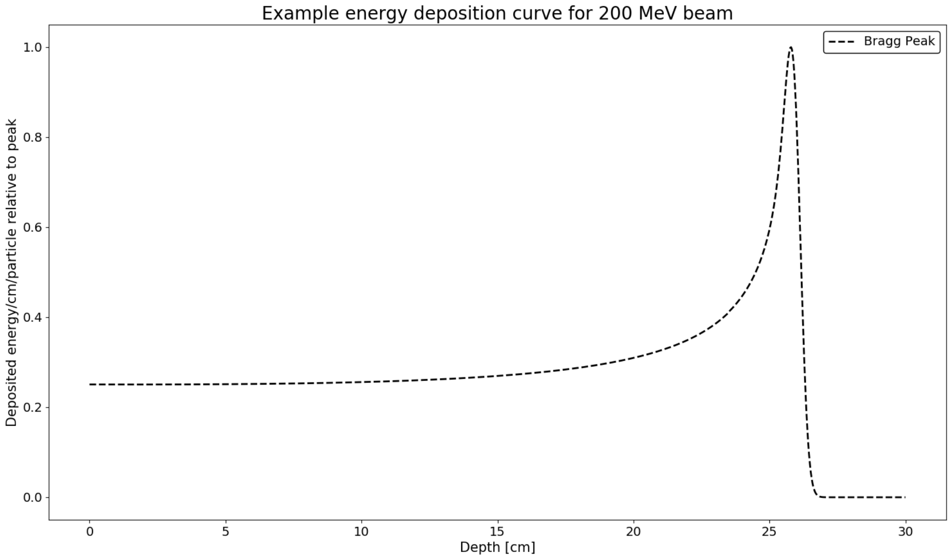

Figure 3: The analytic Bragg curve described parameterised by Bortfeld [4] for a 200 MeV proton beam.

ions and tissue can cause these particles to fragment downstream of the Bragg peak and there is more uncertainty associated with the effectiveness of heavy-ion radiotherapy. As a result, there is less research into this form of radiotherapy [11]. The dose-depth curve for carbon ions is shown in Fig. 1.

2.3 The Laser-hybrid Accelerator for Radiobiological Applications

The Laser-hybrid Accelerator for Radiobiological Applications (LhARA) is a proposed facility for the study of novel techniques in particle-beam therapy. A render of the facility is shown in Fig. 4.

Despite research into proton beam therapy providing evidence for its advantages over traditional X-ray-based radiotherapy, an understanding of the biological processes which give rise to the perceived therapeutic benefits is lacking. LhARA will reconcile this knowledge-gap by studying the therapeutic benefit of different beam parameters, including time structure, spectral and spatial distributions, dose rates and diameter, in a variety of physical conditions [18]. Initially, the facility will deliver *in vitro* studies using proton beams with energies between 10 and 15 MeV.

Table 1: Summary of parameters and constants required for the analytic approximation of the Bragg curve [4]

Symbol	**Description**	**Value**	**Unit**
Φ_0	Primary fluence		cm^{-2}
ξ	Substitution to simplify expression	$(R_0 - z)/\sigma$	1
z	Depth		cm
R_0	Range	αE_0^p	cm
σ	Width of Gaussian peak	$\sqrt{\left(\sigma_{\text{mono}}^2 + \sigma_{E,0}^2 \alpha^2 p^2 E_0^{2(p-1)}\right)}$	cm
σ_{mono}	Width of Gaussian range straggling	$0.012 R_0^{0.935}$	cm
$\sigma_{E,0}$	Width of Gaussian energy spectrum	$\approx 0.01 E_0$	MeV
p	Exponent of energy range relation	1.77	1
α	Proportionality factor	0.0022	cm MeV^{-p}
E_0	Initial beam energy		MeV
ρ	Mass density of medium		kg cm^{-3}
$\Gamma(x)$	Gamma function	$\int_0^\infty x^{z-1} e^{-x} dx$ [19]	1
$\mathscr{D}(x)$	Parabolic cylinder function	See [20]	1
β	Slope parameter of fluence reduction relation	0.012	1
γ	Fraction of locally absorbed energy released in nonelastic nuclear interactions	0.6	1
ϵ	Fraction of primary fluence contributing to the tail of the energy spectrum	$\approx$ 0.0 - 0.2	1

At a later stage, *in vivo* experiments will be made possible by proton beams with energies up to 127 MeV [18]. To perform such experiments, the dose must be delivered accurately and reproducibly. Localisation of the Bragg peak is also essential in a therapeutic setting: the high dose rate of the Bragg peak means that any misalignment will cause damage to surrounding healthy tissue and under-dose the tumour. Hence, online monitoring and dose verification in the end-station are required [22]. Dose verification will be achieved using two coacting methods: scintillating fibre planes and ionacoustics.

Strands of 250 µm-width scintillating fibers will be arranged side-by-side forming a square and fixed in position with resin. Two such squares will be layered so that the fibers on either square are perpendicular, forming a complete plane. A detector is formed by layering multiple planes. Upon irradiation, the electrons in the scintillating fibers are excited to higher energy levels. The relaxation of electrons from this excited state produces visible fluorescence light [23]. Subsequently, total internal reflection within the fibre enables the light to propagate down the fibre where it is captured by a camera and read-out. Using post-processing techniques and accurate calibration, the location and intensity of the energy deposition can be computed.

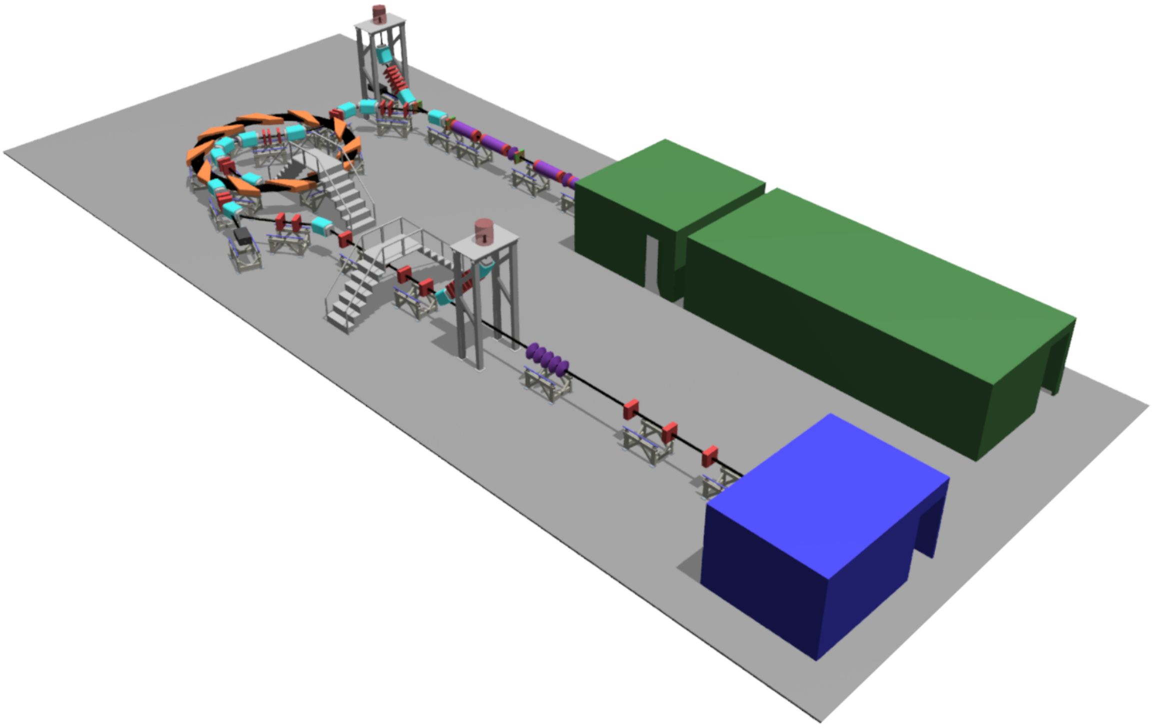

Figure 4: A render of the proposed LhARA facility. Image from [21].

Scintillating fibers were chosen as they can be constructed with a small sensitive volume and have a composition similar to that of tissue [24].

For measuring the energy deposition within tissue, these scintillating fibers are impractical. There is a need for a non-invasive dose verification method: ionacoustics. This emerging technique consists of an array of detectors positioned around the Bragg peak. Details of how this technique attempts to achieve Bragg peak localisation can be found in Section 2.4.

2.4 Ionacoustic imaging

2.4.1 From proton to acoustic wave

Acoustic waves are emitted from the stopping of ionising radiation in matter. These waves have amplitudes directly proportional to the energy deposition of the radiation, enabling the direct measurement of the dose profile in the target [25]. For proton and ion beam therapy, this allows for the mapping of the width, position, and amplitude of the Bragg peak.

The formation of acoustic waves begins with the primarily electromagnetic interaction between protons and matter. These interactions decelerate the protons, which consequently deposit of some or all of their energy in matter. This energy deposition leads to a local temperature increase and subsequent thermal expansion of matter [26]. This thermal expansion produces a detectable pressure pulse.

The propagation of the induced pressure $p(\mathbf{r}, t)$ in water due to a transient temperature increase $T(\mathbf{r}, t)$ is governed by the equation

$$\left(\nabla^2 - \frac{1}{v_s^2}\frac{\partial^2}{\partial t^2}\right) p\left(\mathbf{r}, t\right) = -\frac{\beta}{\kappa v_s^2}\frac{\partial^2 T\left(\mathbf{r}, t\right)}{\partial t^2}, \tag{2}$$

where v_s is the acoustic speed of sound in water, β is the coefficient of volumetric expansion and κ is the isothermal compressibility [26]. Thermal confinement implies that the time for heat diffusion to occur is much greater than the time for protons to stop. Stress confinement is satisfied if the proton pulse is much shorter in duration than the pressure induced volume expansion. By assuming that both these confinement conditions are satisfied, the heat equation can be rewritten as

$$\rho c_V \frac{\partial T(\mathbf{r}, t)}{\partial t} = H(\mathbf{r}, t), \tag{3}$$

where ρ is the mass density, c_V is the specific heat capacity at constant volume, and $H(\mathbf{r}, t) = Q(\mathbf{r})H'(t)$ is the spatially and temporally separable heating function. Hence, Equation 2 can be solved to find

$$p(\mathbf{r}, t) = \frac{\beta}{4\pi v_s \kappa \rho c_V}\frac{\partial}{\partial t}\int_{A(t)}\frac{Q(\mathbf{r}')}{R}dA', \tag{4}$$

where $Q(\mathbf{r}')$ is the deposited energy density, $R = |\mathbf{r} - \mathbf{r}'|$, and $A(t)$ is the surface over which $R = v_s t$ [26]. These acoustic pressure waves generate an electrical signal as a function of time, called as the time-series, at a transducer. The time-series is used to reconstruct the initial pressure distribution. Mathematically, the pressure vector $\mathbf{P}$ at a given set of positions and times can be expressed as

$$\mathbf{P} = M \cdot \mathbf{f}, \tag{5}$$

where $\mathbf{f}$ is the absorption vector, or the absorption per unit volume and M is the model matrix which governs the relationship between the deposited energy and the pressure waves detected at the transducer [27]. Equation 5 assumes that the transducer acts as a point detector. In reality, the detector has finite size, with the signal being spatially averaged over the area of the detector. This is corrected for by considering the detector as a collection of discrete surface elements or by determining the spatial impulse response of the detector, which is a function of its geometry [27].

The sensitivity and resolution of the detector is dependent on its intrinsic frequency response, which should be tailored to be sensitive to the frequency content of the given beam [27]. Ionacoustic waves have variable frequency content which is dependent on the energy and spatial and temporal dose distribution of the beam.

2.4.2 Iterative time reversal image reconstruction

In principle, it is possible to infer the initial pressure distribution based on the signal received at the detector using image reconstruction methods originally developed for photoacoustic imaging. Photoacoustic imaging differs from ionacoustic imaging in that it images optical energy deposition rather than that of protons and ions. Many different image reconstruction algorithms exist, including universal back-projection, Fourier transform, (iterative) time reversal and inversion of the linear Radon transform [28][29][30][5][31]. This report focuses on the iterative time reversal reconstruction method. The challenge of ionacoustic image reconstruction is to recover the three-dimensional spatial pressure distribution due to the energy deposition of an ion or proton beam, coined the initial pressure distribution $p_0(\mathbf{r})$, based on data measured with detectors on a surface S over between time $t = 0$ and $t = T$. Time reversal is based on the principle that the wave equation is invariant under the transform time $t \rightarrow -t$ [32]. To find p_0, one can retransmit the data measured at S in a time-reversed form using the time-reversed variable $\hat{t} = T - t$ over a period with t running from $T \rightarrow 0$ (so $\hat{t}$ runs from $0 \rightarrow T$) [33] [34]. Mathematically, this is achieved by imposing the measurements at S between $t = 0$ and $t = T$ as the time varying Dirichlet boundary conditions [34]. To achieve this, we must assume that for $\hat{t} = 0$ the pressure on S, p_S, is zero. Hence, T must be chosen such that all the waves from

p_0 have left the observable domain (i.e. the volume in which waves could feasibly be allowed to propagate to S). Assuming S has odd dimensions and that the sound speed is constant, Huygens' principle states that for any initial source with bounded support and for any bounded domain, there exists a time when the wave propagating from the initial source will leave the domain. Hence, the use of time reversal is subject to the conditions that the sound speed is constant, the dimensions of S are odd, and that the initial source has bounded support and domain [35]. To minimize the error between the initial and reconstructed pressure distribution, an iterative time-reversal reconstruction procedure can be used [36]. Fig. 5 is a flow-chart describing the iterative procedure.

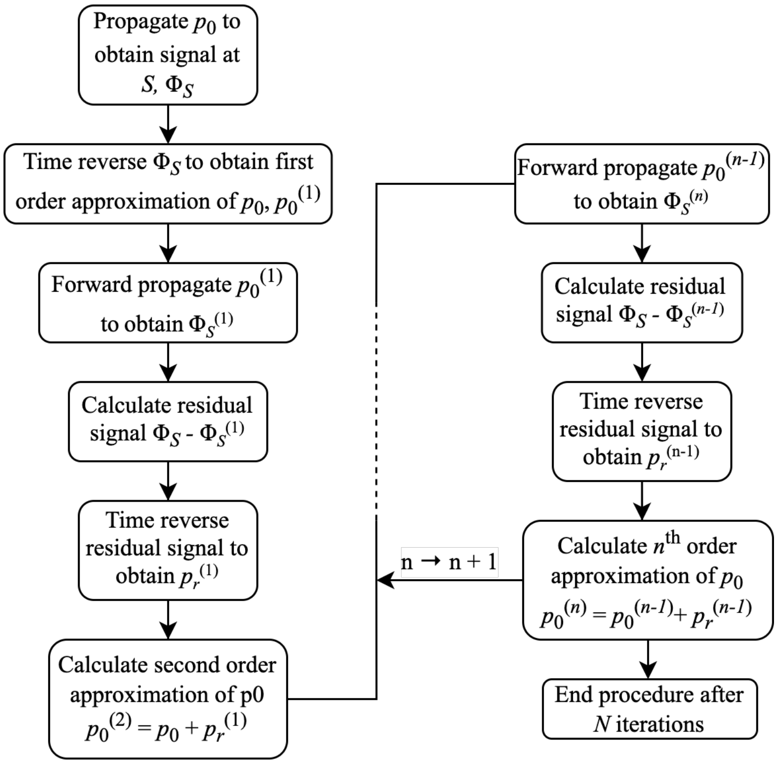

Figure 5: Flow chart explaining how the iterative time reversal procedure is executed. p_0 is the initial pressure distribution, S is the surface of the detector, ϕ_S is the signal at the detector, $\phi_S^{(n)}$ is the signal at the detector calculated by propagating the nth order reconstruction of p_0, $p_0^{(n)}$, the residual signal is the difference between the signal actually detected at the detector and the signal due to the n^{th} order reconstruction, $p_r^{(n)}$ is the pressure distribution calculated by retransmitting the residual signal, N is the total number of iterations performed. The N^{th} order reconstruction of p_0 is given by the expression $p_0^{(N)} = p_0^{(N-1)} + p_r^{(N-1)}$.

2.5 Similar studies

Ionacoustic dose mapping for proton beams is an active area of research. Orukari et. al., 2021 [37] demonstrates k-Wave's ability to simulation the acoustic propagation of the pressure waves from a proton. They suggest that the transducers used to detect ionacoustic signals require sensitivity in low frequency ranges. Ionacoustic image reconstruction of a proton beam is achieved in Lascaud et. al., 2021 [38] using a linear sensor array. In Assmann et. al., 2015 [2], k-Wave simulations were used in conjunction with experiment, establishing that Bragg peak by a low energy proton beam (20 MeV) was able to be localised with accuracy $< 100\,\mu\text{m}$. They do not achieve this using reconstruction methods, as is done in this work, but rather by analysing the time-series of the detector measurements. Techniques to improve signal-to-noise ratio in ionacoustic experiments are tested in Lascaud et.al., 2021 [39], with promising results suggesting that contrast agents optimise data collection. In Kellnberger et. al., 2016 [40] a backprojection algorithm is used to experimentally achieve 3D ionacoustic tomography.

3 Methods

To demonstrate the performance of ionacoustics to reconstruct the dose profile of a proton beam, the simulation and reconstruction of a proton beam in water was investigated. An overview of this simulation procedure is shown in Fig. 6.

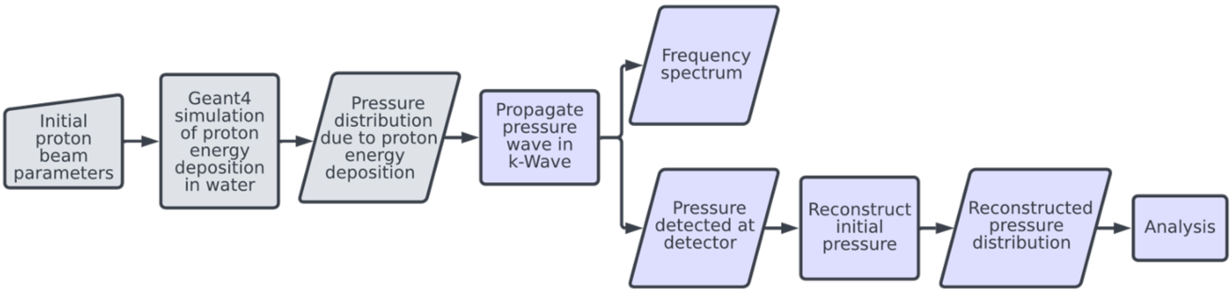

Figure 6: An outline of the simulation pipeline used for this project. The boxes in purple were steps design and carried out as part of this project.

3.1 Initial proton beam parameters

A test proton beam was chosen to be similar to beams that will be used in experiments at the LhARA facility [18]. The 200 MeV test beam consists of 10^4 protons. The lateral profile of the beam is elliptic. A summary of the beam parameters is shown in Table 2.

Table 2: Summary of beam parameters of test beam used for simulations

Property	**Mean value**	**Standard deviation**	**Minimum**	**Maximum**	**Unit**
Energy	200	2	192	208	MeV
X position	0	0.74	-1.66	1.64	mm
Y position	0	2.34	-5.24	5.21	mm
Normalised X momentum	0	0.4	-1.0	1.0	e-3
Normalised Y momentum	0	1.6	-3.5	3.5	e-3

3.2 Geant4 simulation

Geant4 is a C++-based toolkit which uses stochastic Monte Carlo techniques to model the interaction of particles with matter. The Geant4 simulation used in this project, dubbed the

SmartPhantom, was devised by H.T. Lau [41]. A 30 × 30 × 30cm water phantom was modeled in Geant4, as shown in Fig. 7. The model phantom used in this simulation does not include the plexiglass walls surrounding the phantom, but more recent versions of the SmartPhantom can be modified to include this.

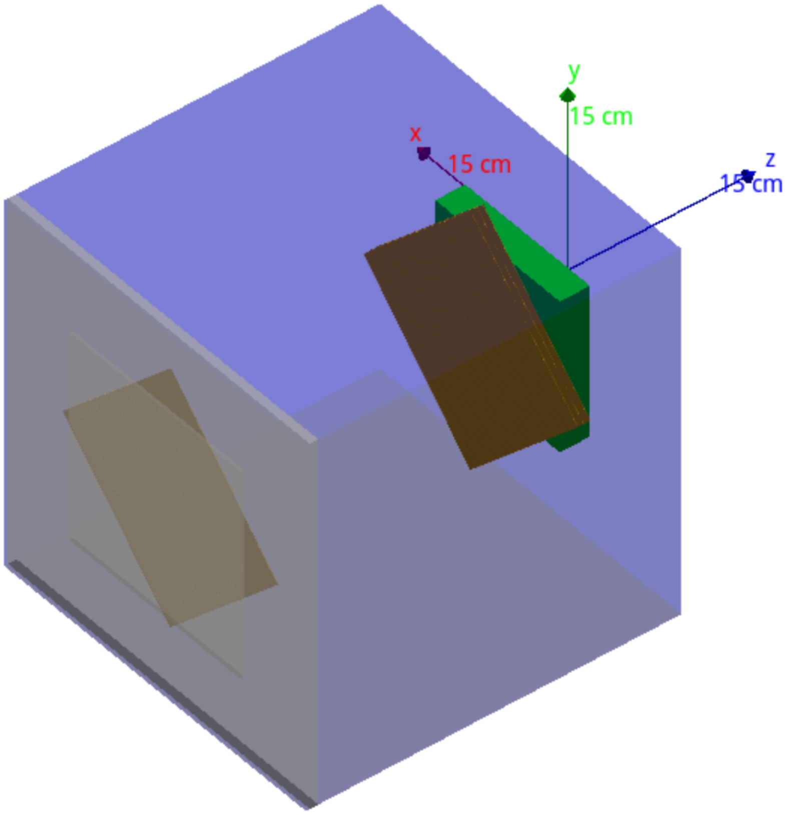

Figure 7: Render of the SmartPhantom used in the Geant4 simulation. The brown planes represent the scintillating fibres. The blue colour shows the volume of water. The grey plane represents the plexiglass window, which was not included in the simulations used for this work. Image from [41].

The test beam described in Section 3.1 was centred in the phantom at $x = y = 0$ and travelled in the positive z direction. The particles are sent into the phantom with a time delay. However, only the final dose distribution, which is invariant with respect to any time structure of the beam, is used in the project.

The SmartPhantom simulation ultimately produces a file containing the location and intensity of the energy deposited by each particles composing the beam.

3.3 Post Processing

The energy deposition profile produced by the SmartPhantom must be transformed into a format compatible with MATLAB-based acoustic simulation software. This post-processing is carried out in C++. First of all, the energy deposition data must be voxelised. The user can change the number of voxels the $30 \times 30 \times 30$cm phantom is divided into by choosing the number of segments in each of the x, y and z directions. In the current version of the SmartPhantom, each direction must be divided into the same number of voxels. Finally, the voxelised data is transferred to a MATLAB input file. For this work, cubic voxel sizes of 10 mm and 5 mm width were chosen. This choice was made due to the excessive computational time taken for simulations with smaller voxel widths.

3.4 k-Wave

k-Wave is an open-source acoustic modeling toolbox for MATLAB [5]. Given an initial pressure distribution, it is able to simulate the propagation of acoustic waves through a medium. It is also possible to simulate detectors and implement time-reversal and Fourier image reconstruction using k-Wave.

3.5 Experiment design

To determine whether an ionacoustic detector could be used to reconstruct an initial pressure distribution, a simulation was set up in k-Wave.

A visualisation of the experiment design is shown in Fig. 8. As to remain consistent with the Geant4 simulation, the pressure distribution is travelling along the z direction, centred about $x = y = 0$ in the x-y plane. A hemispherical detector made up of single-voxel point detectors was positioned on axis with the beam, such that it is concave in the $-z$ direction and convex in the $+z$ direction. The hemisphere was created using k-Wave's `makeBowl` function [5]. Ideally, a surface fully enclosing the initial pressure distribution would be used to perform time-reversal reconstruction, as this is a condition of time-reversal image reconstruction. Given the practical limitations of the detector prototype, which must accommodate scintillating fibre planes, a hemisphere was chosen as a compromise. A planar detector geometry was considered as an alternative to a hemisphere. However, unlike a hemispherical sensor, a planar sensor does not provide information about the 3D structure of the beam, and thus is prone to limited view artefacts. Ultimately, the hemispherical geometry was chosen as a trade-of between practicality and imaging the 3D structure of the beam.

The initial grid size from the initial energy deposition distribution was either $30 \times 30 \times 30$ voxels (for 10 mm voxel size) or $60 \times 60 \times 60$ voxels (for 5 mm voxel size). However, in order to accommodate larger detectors, the grid size was increased to $46 \times 46 \times 46$ voxels (for 10 mm voxel size) and $92 \times 92 \times 92$ voxels (for 5mm voxel size) by adding a layer of 16 (for 10 mm voxel size) or 32 (for 10 mm voxel size) zero voxels around the initial pressure distribution, to form the whole computational grid.

First, the initial energy distribution was converted to energy density by dividing by the voxel volume. Next, the energy density was transformed to the intial pressure distribution p_0 by multiplying by the dimensionless Grüneisen (0.11 for water [42]). The Grüneisen expresses the relationship between the thermal (i.e. energy) and mechanical (e.g. pressure) properties of matter [43]. Following this, p_0 was propagated using the `kspaceFirstOrder3D` function for a time $(N_x \times dx)/c$ where N_x is the number of voxels, dx is the voxel width in m and c is the speed of sound in water ($1500\,\mathrm{m\,s^{-1}}$).

The pressure detected at the hemispherical detector was used to reconstruct the initial pressure distribution, using the iterative time-reversal method described in Section 2.4.2. This is implemented in k-Wave by passing the measured data to the `sensor.time_reversal_boundary_data` parameter which is a property of the `sensor` object, which defines the detector. Then, by calling `kspaceFirstOrder3D`, k-Wave will compute the time-reversed reconstructed signal based on the measured data.

To determine the configuration of the sensor which best reconstructs the initial pressure distribution, the following specifications of the sensor were varied:

- Sensor diameter d;
- Sensor z-position z_d;
- Number of iterations in time-reversal imaging N;
- Voxel dimensions.

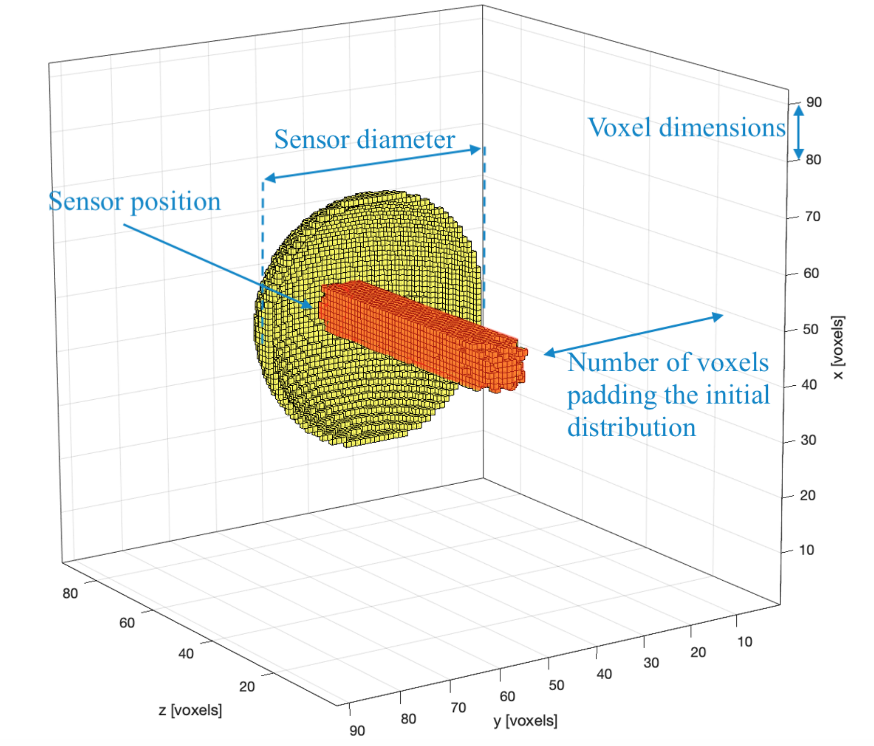

Figure 8: Visualisation of the simulation set-up. The hemispherical detector is depicted with yellow voxels. The red voxels represent the voxels with non-zero initial pressure. The beam is travelling in the $+z$ direction, away from the viewer. The sensor position is defined as the base of the bowl, as indicated by the arrow. The sensor diameter and zero-padding voxels are indicated on the diagram. The arrow marked ‘voxel dimensions’ extends across 10 voxels.

The radius of curvature of the sensor was defined to be $d/2$ in order to preserve a hemispherical shape. Fig. 8 shows these parameters in a render of the simulation set-up.

4 Results and Discussion

4.1 General notes on the reconstruction performance

Fig. 9 shows an example of a reconstructed Bragg peak for a detector with $d = 35\,\mathrm{cm}$, voxel width $= 10\,\mathrm{mm}$, $z_d = 35\,\mathrm{cm}$, $N = 10$. The Bragg peak is captured well by the reconstruction, however the plateau of the Bragg curve downstream of the peak is not reconstructed at all. This feature of the reconstructed is visible across all reconstructions. Fig. 10 shows the longitudinal profile of this reconstruction alongside that of the initial distribution.

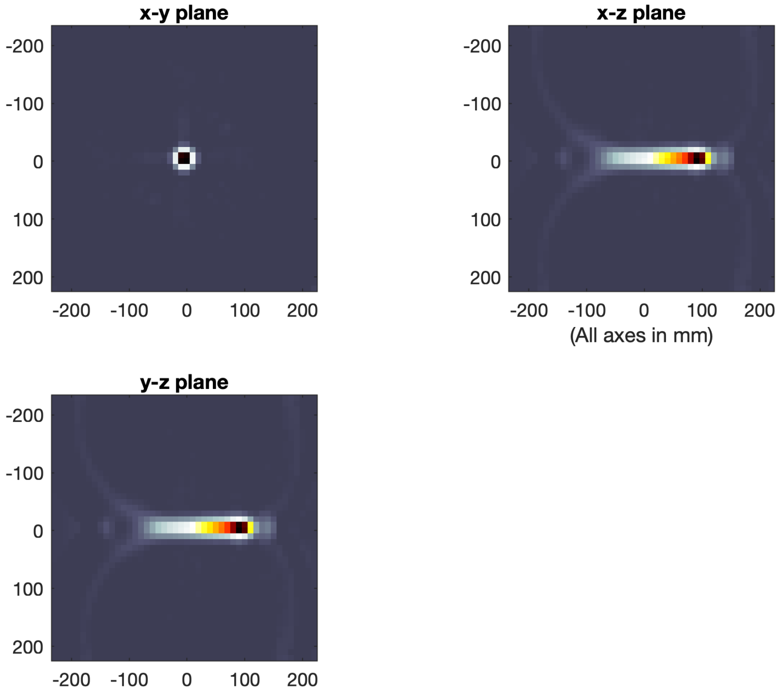

Figure 9: Reconstructed pressure distribution for a sensor with $d = 35\,\mathrm{cm}$, voxel width $= 10\,\mathrm{mm}$, $z_d = 35\,\mathrm{cm}$, $N = 10$. The beam is travelling from the left to right of the $x - z$ and $y - z$ plane plots. The Bragg peak is captured by the reconstruction, however the dose upstream of the peak is not well captured. The curved artefacts occur because the detector only partially encloses the initial pressure distribution [34]

To parameterise the initial and reconstructed distributions, the data was fitted with Equation 1. The full-width at half-maximum (FWHM) of the fit was calculated for the initial and reconstructed distributions. The relative error between the initial and reconstructed FWHM

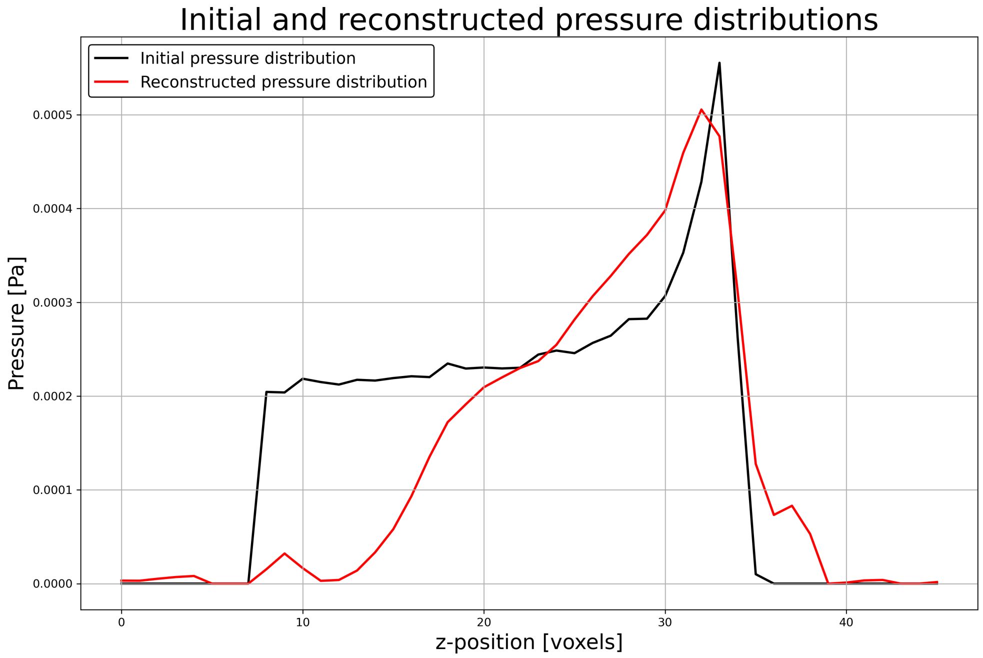

Figure 10: The initial (black) and reconstructed (red) pressure distribution in the longitudinal direction. The reconstructed Bragg peak is much wider than that of the initial distribution. The pressure in the plateau upstream of the beam is not captured in the reconstruction.

was calculated as

$$\Delta\text{FWHM} = \frac{\text{FWHM}_r - \text{FWHM}_i}{\text{FWHM}_i} \times 100\%, \tag{6}$$

where the subscript r and i indicate the reconstructed and initial distributions, respectively. The relative uncertainty associated with ΔFWHM, $\delta_{\Delta\text{FWHM}}/\Delta\text{FWHM}$ was assumed to be the same as the relative uncertainty of σ derived from the curve fit. The error on the location of the Bragg peak was determined by finding the z-position of the maximum of the fitted curves and calculated as

$$\Delta z^{\max} = \frac{z_r^{\max} - z_i^{\max}}{z_i^{\max}} \times 100\%, \tag{7}$$

where $z^{\max}$ is the z-position of the maximum of the fitted curve and subscripts r and i indicate the reconstructed and initial distributions, respectively. The relative uncertainty on $\Delta z^{\max}$, $\delta_{\Delta z^{\max}}/\Delta z^{\max}$ was assumed to be the same as the relative uncertainty on R_0 derived from the fit. The approach of varying the fit parameters given in Table 1 within their associated uncertainties, then finding the minimum and maximum possible values of $\Delta z^{\max}$ and ΔFWHM would have been the preferred route to obtain $\delta_{\Delta z^{\max}}$ and $\delta_{\Delta\text{FWHM}}$. However, Equation 1 is sensitive to variations in its many parameters, so the input parameters easily become out of the domain of those allowed by Equation 1, ruling out this method of uncertainty calculation.

As seen in Fig. 10, the reconstructed peak is spread out in the z-direction due to the fact that the plateau is not captured. This is why the value σ was not chosen to represent the width of the Gaussian peak - this would be an overestimate - and the FWHM described above was used. The peak position was also subject to a systematic shift towards the $-z$ direction in the reconstructed pressure. This could be due to the reconstruction algorithm assuming that all of the pressure measured at the detector comes from within the detector's field of view (FOV). However, the acoustic propagation from the dose distribution upstream of the Bragg peak, outside of the detector's FOV, is measured by the detector. Since the algorithm will not attribute this pressure to its true location (outside of the detector's FOV), it may attribute this to the most upstream location within its field-of-view. As a result, the z position of the Bragg peak can be thought as as being biased towards the $-z$ direction. Otherwise put, the reconstructed peak is being pulled away from the detector.

In Sections 4.2, 4.3 and 4.4, the relationship between ΔFWHM and Δz^{max} and the number of iterations N, z-position of the detector z_d and the diameter of the detector d are presented. Frequency spectra and time-series of the detector measurements are compared in order to propose explanations for these trends.

4.2 Varying iteration number

When varying N, $d = 31\,\mathrm{cm}$ and $z_d = 42\,\mathrm{cm}$ were held constant. Fig. 13 shows the reconstructed pressure distribution and fit to Equation 1 using between 1 and 30 iterations. The variation of the percentage error on the FWHM of the Bragg peak with iteration number is shown in Fig. 11. The uncertainties associated with the FWHM error are too large to draw any conclusive trends from the data. However, we do see that the gross over-estimate of the FWHM for $N = 1$ is brought down in the following iterations. ΔFWHM derived from the error on the fitted parameter σ. It is clear from Fig. 13, that Equation 1 does not closely match the data, principally due to the uncaptured pre-peak plateau region. Equation 1 is not designed

Figure 11: Variation in the percentage error in the full-width at half-maximum of the Bragg peak with N. Constant d= 31 cm, voxel width = 10 mm, and z_d = 42 cm.

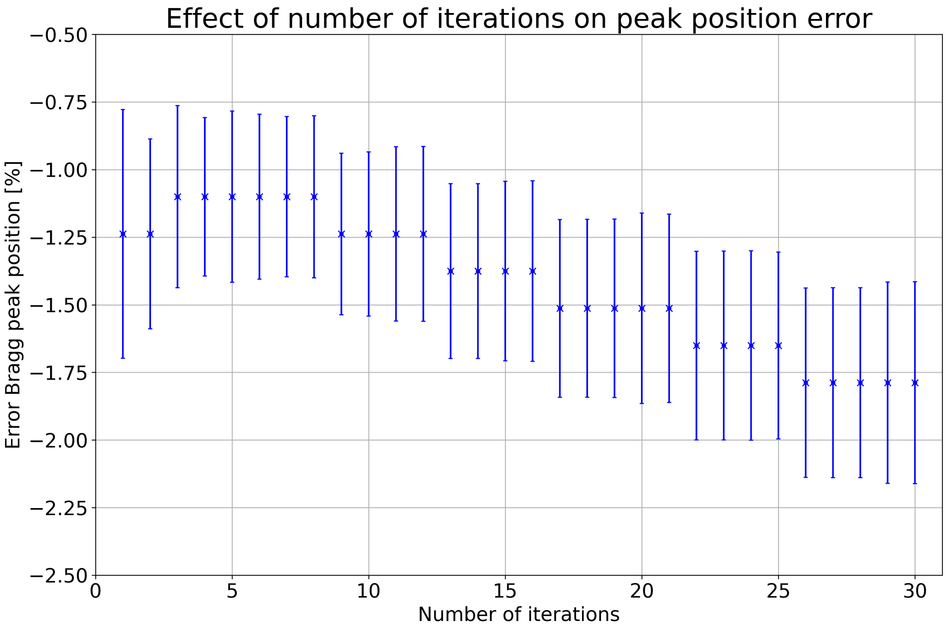

Figure 12: Variation in the percentage error in the Bragg peak position with N. Constant d =31 cm, voxel width = 10 mm and z_d = 42 cm.

to parameterise such a fit, which explains the inability to precisely determine the FWHM. Fig. 12 shows how the percentage difference in the Bragg peak position compared to the initial

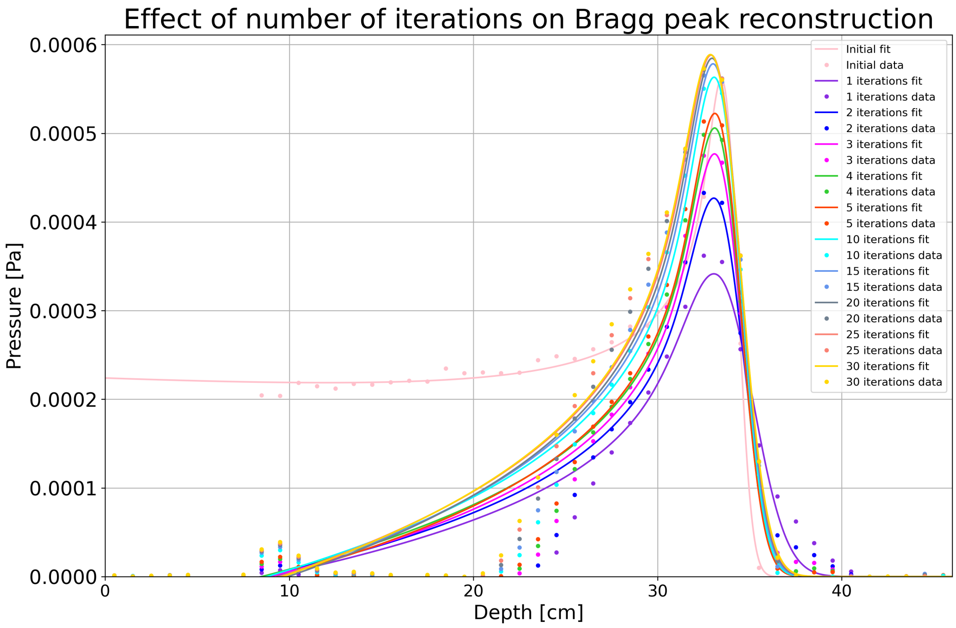

Figure 13: Reconstructed pressure distributions with N varying from 1 to 30. These have been fit with Equation 1. The initial pressure distribution and corresponding fit is shown in light pink. Constant $d = 31\,\text{cm}$, voxel width $= 10\,\text{mm}$, and $z_d = 42\,\text{cm}$.

distribution varies with iteration number. Again, the error bars are too large to validate a trend for the reasons explained above. However, the error appears to remain constant in groups of 2 to 5 successive iterations. As described in Section 4.1, the reconstruction is unable to align the reconstructed Bragg peak with the peak of the initial pressure distribution. This is thought to be due to the detector FOV preventing the pre-peak plateau from being captured, leading to the reconstruction algorithm assigning more pressure just upstream of the actual peak, and broadening the peak as a whole. It is evident from Fig. 13 that an accurate reconstruction of peak's amplitude benefits from more iterations. However, it appears that after ~ 10 iterations the amplitude is over-estimated. This is likely due to pressure waves originating from the pre-peak plateau being wrongly attributed to the Bragg peak. The trends seen in Lascaud et.al., 2021 [38] are not visible in the results presented here, suggesting that this analysis would benefit from a finer grid spacing and alternative detector configuration, more similar to those presented in Lascaud et.al., 2021.

4.3 Varying z-position of detector

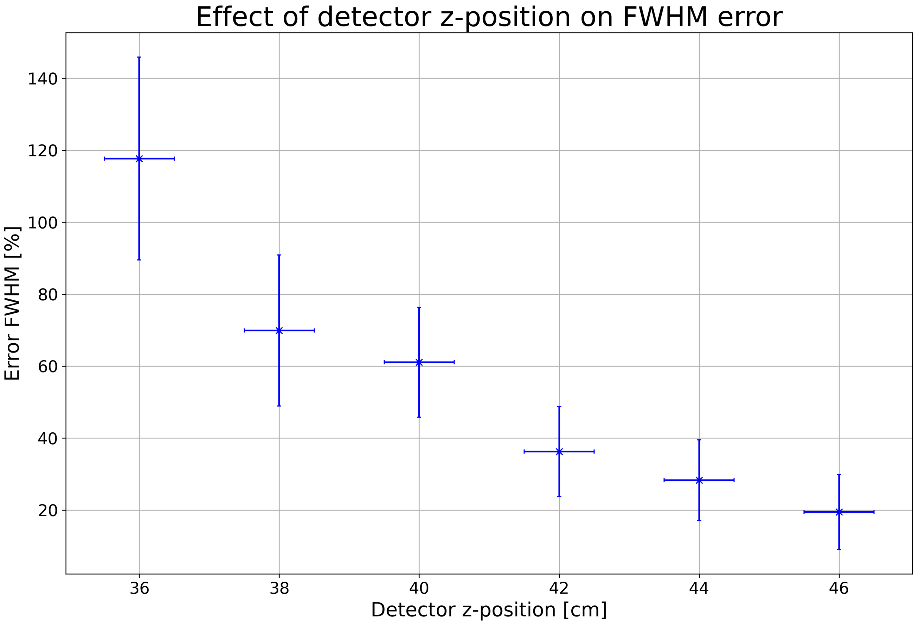

Figure 14: Variation in the percentage error in the full-width at half-maximum of the Bragg peak with the z_d. The x-axis shows the z-position of the detector, where $z = 0$ corresponds to the position of the entry window of the water phantom. Constant $d = 45\,\text{cm}$, voxel width $=$ $10\,\text{mm}$ and N=10.

When varying z_d, $d = 45\,\text{cm}$ and $N = 10$ were held constant. Fig. 16 shows the reconstructed pressure distribution for varying z_d. It can be seen that for detector positions closer to the Bragg peak, more of the plateau of the distribution is captured. This is expected, as the detector's coverage of the beam plateau will increase as the detector is shifted in the $-z$ direction. The percentage error on the FWHM of the Bragg peak as a function of z_d is shown in Fig. 14. The further away the detector is from the Bragg peak appears to correlate with a more accurate Bragg peak FWHM. However, it should be noted that the minimum error $\Delta\text{FWHM} = 20\%$ remains significant. The trend of improving ΔFWHM as the detector is moved away from the Bragg peak is also seen in Lascaud et. al., 2021 [38], however they see an initial underestimation of the FWHM, rather than the overestimation found in this study. Lascaud et. al., 2021 suggests this improvement could be due to the detector sensing more spherical wavefronts at a greater distance from the peak. The uncertainty on ΔFWHM, $\delta\Delta$FWHM, also decreases as the detector is moved in the $+z$ direction. It is not well understood why this may be the case,

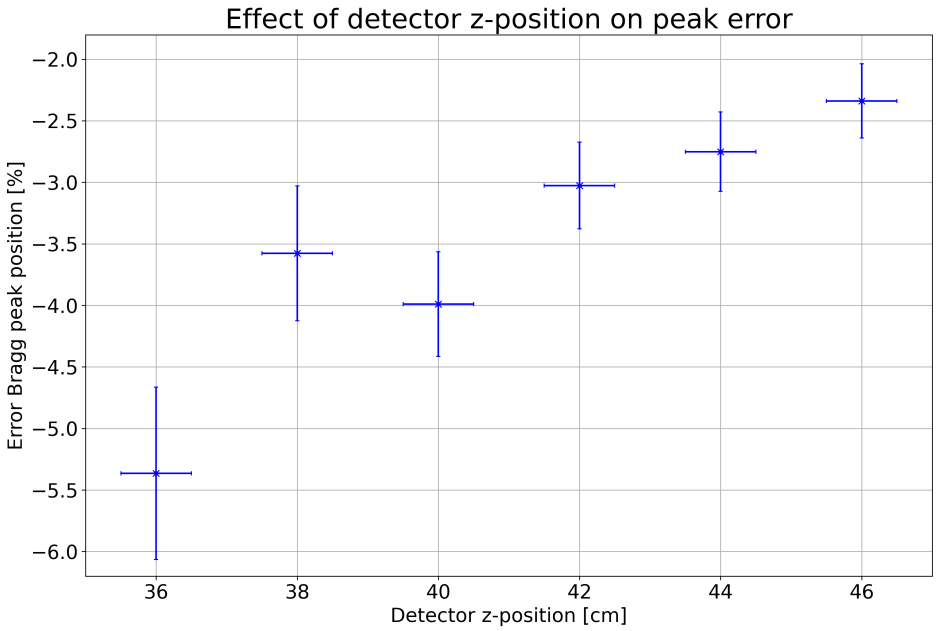

Figure 15: Variation in the percentage error in the Bragg peak position with z_d. The x-axis shows the z-position of the detector, where $z = 0$ corresponds to the position of the entry window of the water phantom. Constant d= 45 cm, voxel width = 10 mm, and N= 10.

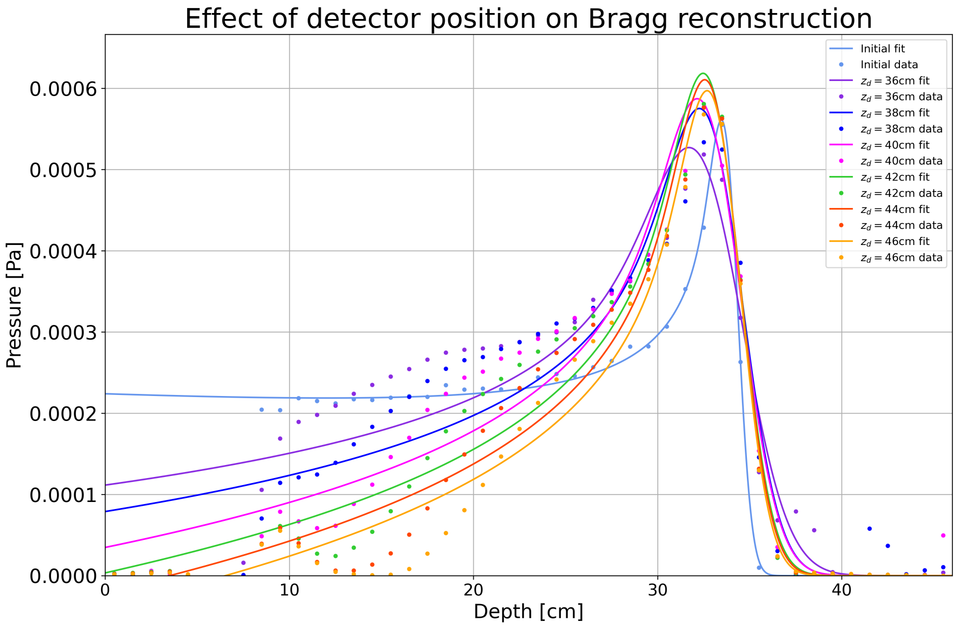

Figure 16: Reconstructed pressure distributions with z_d varying from 36 cm to 46 cm. These have been fit with Equation 1. The initial pressure distribution and corresponding fit is shown in light blue. Constant d = 45 cm, voxel width = 10 mm, and N= 10.

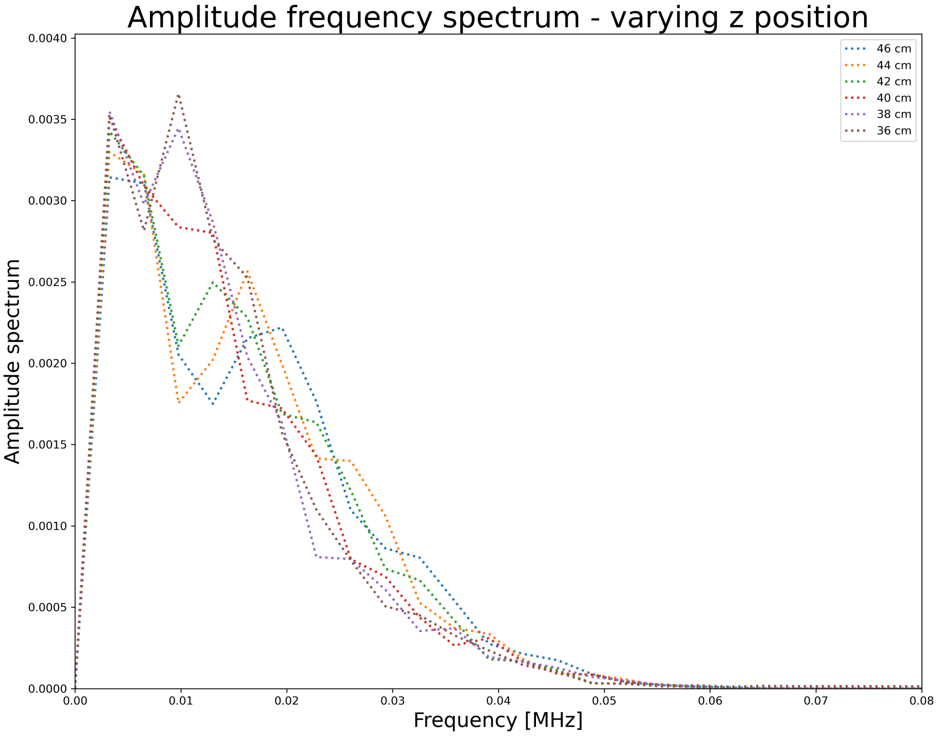

Figure 17: Amplitude frequency spectra for detectors with varied z position. Constant d = 45 cm, the voxel width = 10 mm, and N= 10.

although it is possible this is also explained by the detection of more spherical wavefronts for increased z_d, leading to a better fit of the data. Fig. 15 shows the influence z_d has on the ability for the reconstructed pressure to accurately locate the position of the Bragg peak. The underestimate of the peak position is improved by moving the detector further from the Bragg peak, which is consistent with the results obtained by Lascaud et. al., 2021. Again, this is thought to be due to the detection of more spherical waves for detectors with greater z_d.

Fig. 17 depicts the evolution of the amplitude frequency spectrum as the detector position is varied. When the detector is further away from the Bragg peak, the amplitude peak at 0.01 MHz, visible in the z_d = 36 cm and 38 cm spectra, is suppressed. Moreover, the initial peak in the amplitude frequency spectra at 0.005 MHz reduces in amplitude as the detector is moved away from the Bragg peak. This suggests that the acoustic waves at these frequencies are not reaching the detector when it is positioned further from the Bragg peak. This could be due to the detector enclosing less of the beam when it is further from the Bragg peak, meaning more waves are able to propagate away from the source without being measured by the detector.

There is a distinct dip in the amplitude at ∼0.007 MHz for the 36 cm and 38 cm detectors. The two peaks either side of this dip may be the result of acoustic waves propagating from the Bragg peak (right peak on amplitude frequency spectrum) and acoustic waves (left peak on amplitude frequency spectrum) propagating from the pre-peak plateau. The higher energy density of the Bragg peak causes it to act as a source of higher frequency acoustic waves than those from the pre-peak plateau.

4.4 Varying diameter of detector

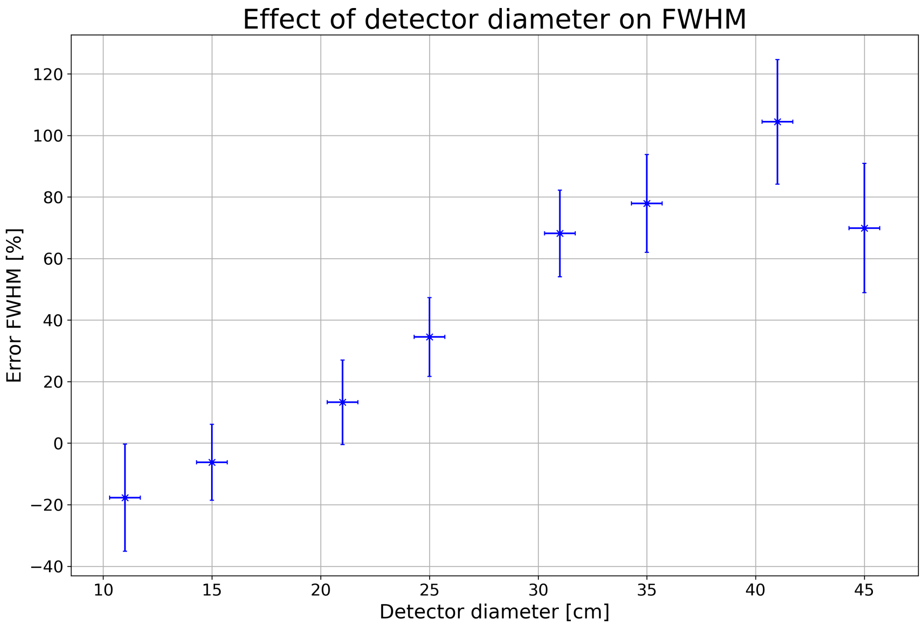

Figure 18: Variation in the percentage error in the Bragg peak FWHM with varying d. Constant voxel width = 10 mm, $z_d = 36$ cm and N= 10.

The diameter of the detector also has an influence on the spatial localisation of the Bragg peak. Fig. 20 shows how the reconstructed data points and corresponding fit depend on the d. For these simulations $z_d = 36$ cm and $N = 10$.

Fig. 21 shows how the shape of amplitude frequency spectrum depends on d. As expected, for

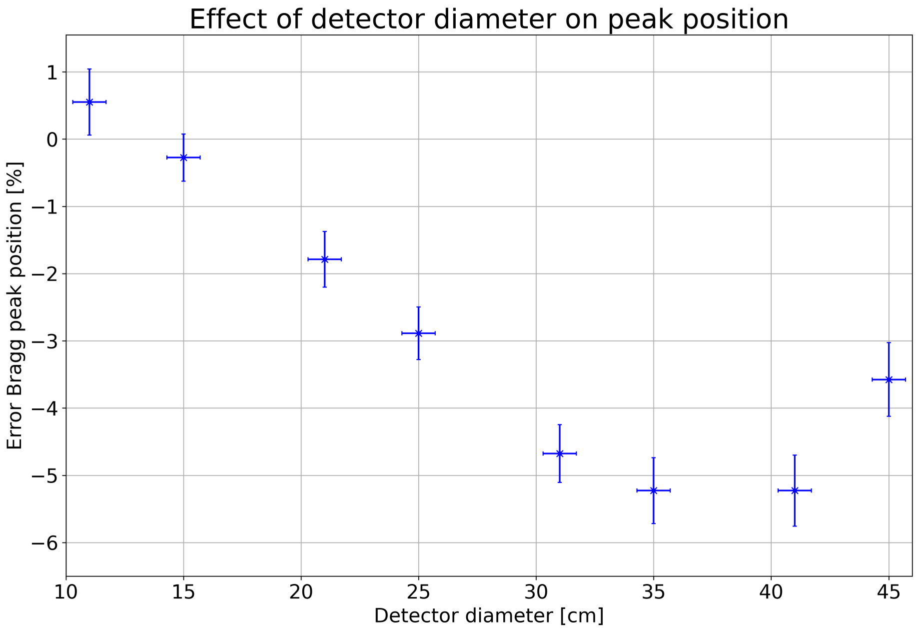

Figure 19: Variation in the percentage error in the Bragg peak position with varying d. Constant voxel width = 10 mm, z_d = 36 cm and N= 10.

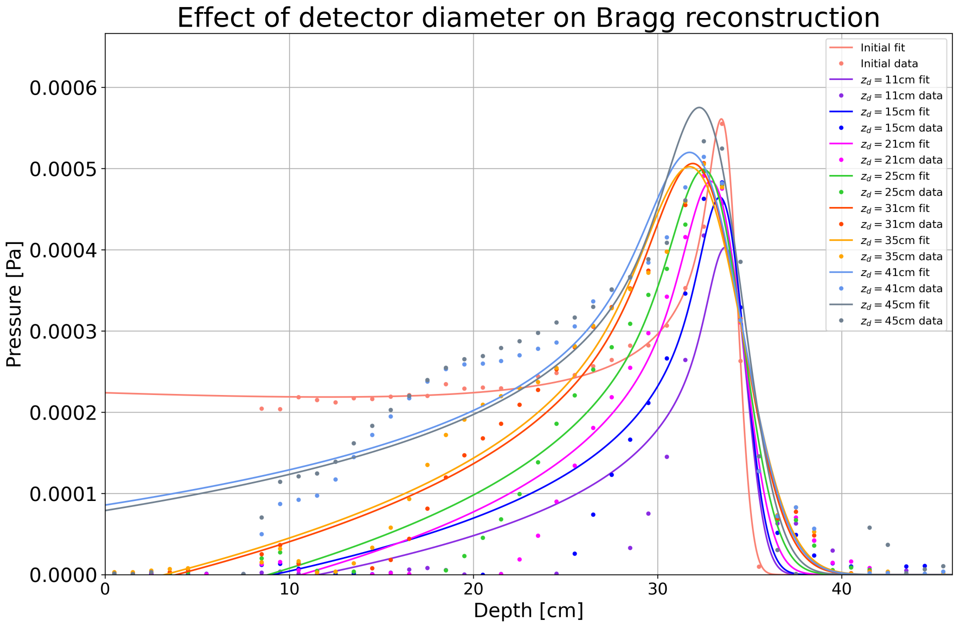

Figure 20: Reconstructed pressure distributions with z_d varying from 36 cm to 46 cm. These have been fit with Equation 1. The initial pressure distribution and corresponding fit is shown in pale pink.

a larger sensor the amplitude frequency spectrum has an increased amplitude: more detectors will accumulate more pressure waves. The dip in amplitude (at 0.01 MHz for d = 41 cm and

45 cm) occurs at a higher frequency for smaller detectors. It is thought that for smaller detector sizes, not enough of the pressure waves are captured by the detector, leading to the 'flattened out' amplitude frequency spectrum visible for $d = 11\,\text{cm}$.

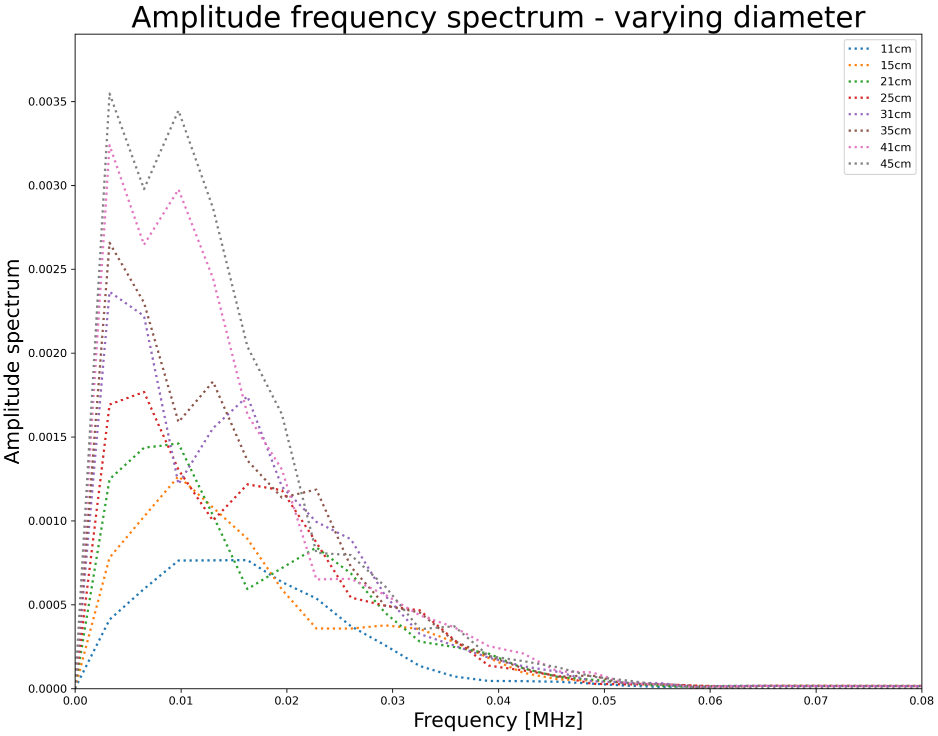

Figure 21: Amplitude frequency spectra for detectors with varied d. Constant $z_d = 45\,\text{cm}$ and voxel width $= 10\,\text{mm}$ for all simulations.

Fig. 22 shows significant artefacts in the lateral reconstructed profile for detectors with $d < 25\,\text{cm}$. While these artefacts are not well understood at this stage, there is a correlation with the change in frequency spectra shape for smaller detectors shown in Fig. 21. Moreover, the time-series at the detector for these reconstructions do not present stark differences to the time-series for reconstructions without lateral artefacts, as shown in Fig. 23. However, it appears that the detector experienced non-zero pressure at $t = 0$ for these simulations, which may have resulted in errors in the reconstruction for small d. It is also possible that resonance within the detector bowl causes these artefacts. Further investigation into the cause of these artefacts and how to avoid them is necessary. The data presented in Fig. 18, Fig. 19 and Fig. 20 are likely inhibited by these artefacts. Fig. 20 shows that the amplitude of the Bragg peak is increased with a larger d, which is expected since the detector will comprise more single-voxel detectors

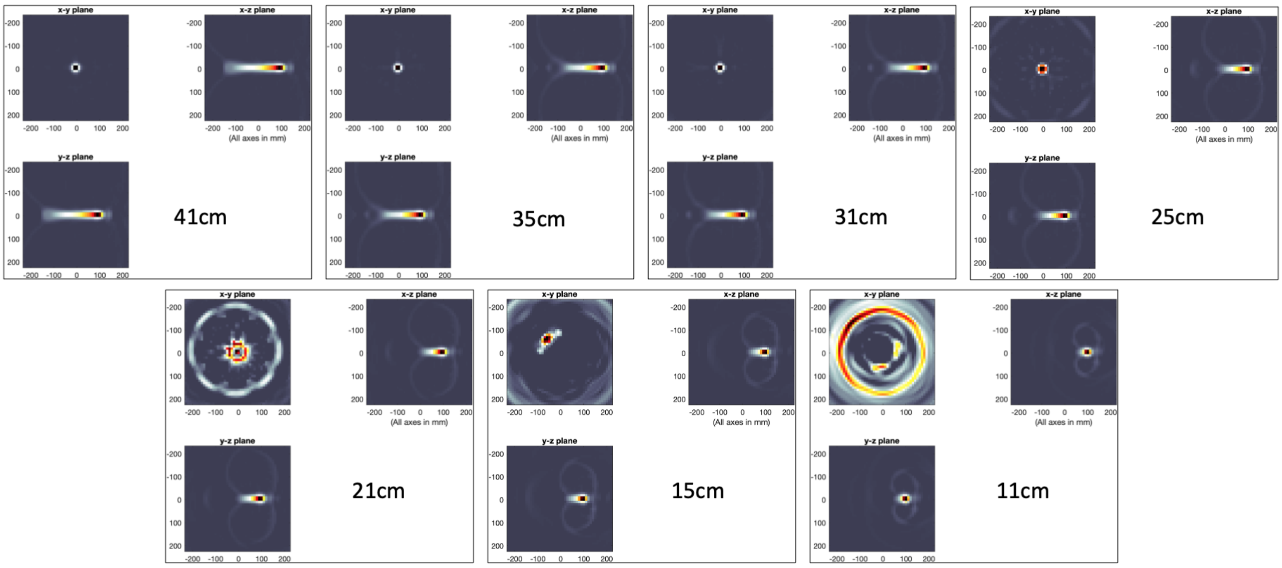

Figure 22: Reconstructed pressure distributions for varying d. Circular artefacts in the x-y plane become pronounced when d is reduced below 31 cm. Constant $z_d = 45$ cm and voxel width = 10 mm for all simulations.

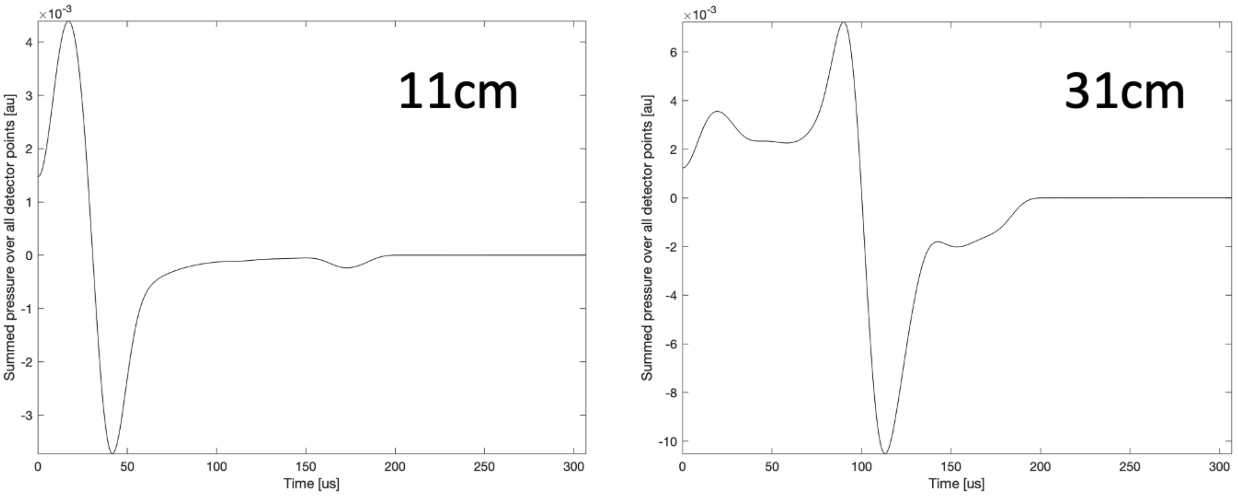

Figure 23: Time series for detectors with $z_d = 36$ cm, $N = 10$, and $d = 11$ cm (left) and 31 cm (right). The detectors experienced non-zero pressure at $t = 0$ for these simulations, which may have resulted in artefacts present in the lateral reconstruction of the initial pressure for smaller d.

and thus capture more amplitude. Hence, combining this understanding with the information acquired in Section 4.2, it appears that a smaller detector may benefit from increased N in order to accurately represent the Bragg peak amplitude. Fig. 18 shows the relationship between d and ΔFWHM. For small d, the FWHM is underestimated. However, as d increases, so does the overestimate on the FWHM. A larger diameter will correspond to a wider FOV for the detector. Hence, the reconstruction algorithm will have more volume in which to attribute the acoustic waves within its field of view, resulting in a greater margin for error. Fig. 19 shows how ΔFWHM varies with *d*. As for Fig. 18, the trend is not well understood, as it would be expected that a larger detector with more elements would be able to collect more information about the Bragg peak position, which is not visible in Fig. 19. More investigation with different sensor configurations is necessary to better understand the artefacts present in these reconstructions, and hence determine clear trends in the data.

5 Conclusions

5.1 Summary of results

PBT enables radiotherapy to be delivered to tumour targets while minimising the damage to surrounding tissue. Ionacoustics is an emerging technique for mapping the dose profile from a proton beam. The use of this technique in the LhARA facility will enable current understanding of the biological mechanisms underpinning PBT to be improved. This work presents the design, implementation and testing of a simulation of the acoustic propagation of pressure waves due to a 200 MeV proton beam, using the k-Wave toolbox. An iterative time-reversal algorithm was used to reconstruct the initial pressure distribution left by the proton beam in a $30\times30\times30$cm water phantom based on the measurements at a hemispherical detector. The initial and reconstructed pressure distributions were fit to the analytic equation given in Bortfeld, 1997 [4] in order to evaluate the performance of the reconstruction. The detector diameter, z-position and the number of iterations used in the reconstruction algorithm were varied to show the relationship between these parameters and the reconstruction performance. Results suggest that a much finer grid size needs to be used to draw insightful conclusions from the simulation. The frequency content measured by the detector was shown to be heavily dependent on the detector geometry.

5.2 Future Work

The work presented in this report indicates a clear direction for future work required in characterising an ionacoustic detector before constructing a prototype for use in the LhARA facility.

Simulation run-time posed a significant constraint in this work, with simulations using a 5 mm voxel width taking ~ 20 min per iteration. As a first measure, the simulation pipeline should be transferred to a cluster to support faster computational times. Faster computational times will facilitate the use of a finer grid size. Convergence testing should be performed for voxel widths

$\leq 1\,\mathrm{mm}$. As proposed in Section 4, the grid size could be the cause of certain reconstruction artefacts. Similarly, convergence testing by reducing the time step used in simulations should be carried out.

Fitting the reconstructed distributions with Bortfeld's parameterisation of the Bragg curve was hindered by the limited view of the reconstructed distributions. The simulated detectors were unable to reconstruct the dose distribution plateau upstream of the Bragg peak. Hence, there is need for the ionacoustic detector to be sensitive to energy deposition in the plateau. Different configurations of detector should be tested to determine how this can be achieved within the practical constraints of the detector design. For example, a cylindrical array surrounding the beam could be trialled.

The detector field of view (FOV) is a parameter not considered explicitly in this work. Finding the relationship between the FOV and Bragg peak error would improve further analysis.

Once the trends in a continuous detector are well understood, the sensor should be divided into spatially separated detector elements. This fragmented detector design is a more realistic representation of the prototype that will be constructed.

Finally, this work employs the iterative time-reversal reconstruction algorithm, however as stated in Section 2.4.2 many other algorithms exist. Comparison of the efficiency and performance of these algorithms should be carried out. Improving the efficiency of the algorithm is key to realising online ionacoustic imaging.

References

[1] E. J. Lehrer, A. V. Prabhu, K. K. Sindhu, S. Lazarev, H. Ruiz-Garcia, J. L. Peterson, C. Beltran, K. Furutani, D. Schlesinger, J. P. Sheehan, and et al., “Proton and heavy particle intracranial radiosurgery,” *Biomedicines*, vol. 9, no. 1, p. 31, 2021.

[2] W. Assmann, S. Kellnberger, S. Reinhardt, S. Lehrack, A. Edlich, P. G. Thirolf, M. Moser, G. Dollinger, M. Omar, V. Ntziachristos, and K. Parodi, “Ionoacoustic characterization of the proton bragg peak with submillimeter accuracy,” *Medical Physics*, vol. 42, no. 2, pp. 567–574, 2015. [Online]. Available: https://aapm.onlinelibrary.wiley.com/doi/abs/10.1118/1.4905047

[3] S. Agostinelli, J. Allison, K. Amako, J. Apostolakis, H. Araujo, P. Arce, M. Asai, D. Axen, S. Banerjee, G. Barrand, and et al., “Geant4—a simulation toolkit,” *Nuclear Instruments and Methods in Physics Research Section A: Accelerators, Spectrometers, Detectors and Associated Equipment*, vol. 506, no. 3, pp. 250–303, 2003. [Online]. Available: https://www.sciencedirect.com/science/article/pii/S0168900203013688

[4] T. Bortfeld, “An analytical approximation of the Bragg curve for therapeutic proton beams,” *Medical Physics*, vol. 24, no. 12, p. 2024–2033, 1997.

[5] B. E. Treeby and B. T. Cox, “k-Wave: MATLAB toolbox for the simulation and reconstruction of photoacoustic wave fields,” *Journal of Biomedical Optics*, vol. 15, no. 2, p. 021314, 2010.

[6] MATLAB, *version 7.10.0 (R2010a)*. Natick, Massachusetts: The MathWorks Inc., 2010.

[7] W. D. Newhauser and R. Zhang, “The physics of proton therapy,” *Physics in Medicine and Biology*, vol. 60, no. 8, p. R155–R209, Mar 2015.

[8] J. Ferlay, M. Colombet, I. Soerjomataram, D. M. Parkin, M. Piñeros, A. Znaor, and F. Bray, “Cancer statistics for the year 2020: An overview,” *International Journal of Cancer*, vol. 149, no. 4, p. 778–789, 2021.

[9] M. Arruebo, N. Vilaboa, B. Sáez-Gutierrez, J. Lambea, A. Tres, M. Valladares, and A. González-Fernández, "Assessment of the Evolution of Cancer Treatment Therapies," *Cancers*, vol. 3, no. 3, p. 3279–3330, 2011. [Online]. Available: https://dx.doi.org/10.3390/cancers3033279

[10] J. J. Wilkens, C. Granja, C. Leroy, and I. Stekl, *Introduction to Radiotherapy with Photon and Electron Beams and Treatment Planning from Conformal Radiotherapy to IMRT*. THE 4TH INTERNATIONAL CONFERENCE ON MATERIALS ENGINEERING AND NANOTECHNOLOGY (ICMEN 2021), 2007.

[11] H. Paganetti, *Proton Beam Therapy*, ser. 2399-2891. IOP Publishing, 2017. [Online]. Available: https://dx.doi.org/10.1088/978-0-7503-1370-4

[12] X. Tian, K. Liu, Y. Hou, J. Cheng, and J. Zhang, "The evolution of proton beam therapy: Current and future status (review)," *Molecular and Clinical Oncology*, 2017.

[13] "Dose-dependent biological damage of tumour cells by laser-accelerated proton beams," vol. 12, p. 085003, Aug 2010.

[14] Y. Prezado and G. R. Fois, "Proton-minibeam radiation therapy: A proof of concept," *Medical Physics*, vol. 40, no. 3, p. 031712, 2013.

[15] Y. Prezado, G. Jouvion, D. Hardy, A. Patriarca, C. Nauraye, J. Bergs, W. González, C. Guardiola, M. Juchaux, D. Labiod, and et al., "Proton minibeam radiation therapy spares normal rat brain: Long-term clinical, radiological and histopathological analysis," *Scientific Reports*, vol. 7, no. 1, 2017.

[16] Y. Prezado, G. Jouvion, A. Patriarca, C. Nauraye, C. Guardiola, M. Juchaux, C. Lamirault, D. Labiod, L. Jourdain, C. Sebrie, and et al., "Proton minibeam radiation therapy widens the therapeutic index for high-grade gliomas," *Scientific Reports*, vol. 8, no. 1, 2018. [Online]. Available: https://dx.doi.org/10.1038/s41598-018-34796-8

[17] P. Chaudhary, T. I. Marshall, F. M. Perozziello, L. Manti, F. J. Currell, F. Hanton, S. J. Mcmahon, J. N. Kavanagh, G. A. P. Cirrone, F. Romano, and et al., "Relative

biological effectiveness variation along monoenergetic and modulated bragg peaks of a 62-mev therapeutic proton beam: A preclinical assessment," *International Journal of Radiation Oncology*Biology*Physics*, vol. 90, no. 1, p. 27–35, 2014. [Online]. Available: https://dx.doi.org/10.1016/j.ijrobp.2014.05.010

[18] G. Aymar, T. Becker, S. Boogert, M. Borghesi, R. Bingham, C. Brenner, P. N. Burrows, O. C. Ettlinger, T. Dascalu, S. Gibson, and et al., "LhARA: The Laser-hybrid Accelerator for Radiobiological Applications," *Frontiers in Physics*, vol. 8, 2020.

[19] E. W. Weisstein, "Gamma Function." [Online]. Available: https://mathworld.wolfram.com/GammaFunction.html

[20] ——, "Parabolic Cylinder Function." [Online]. Available: https://mathworld.wolfram.com/ParabolicCylinderFunction.html

[21] G. Aymar, T. Becker, S. Boogert, M. Borghesi, R. Bingham, C. Brenner, P. Burrows, T. Dascalu, O. Ettlinger, S. Gibson, and et al., 2020. [Online]. Available: https://ccap.hep.ph. ic.ac.uk/trac/raw-attachment/wiki/Communication/Notes/CCAP-TN-01. pdf

[22] A. Kurup, "Diagnostics for LhARA: a Laser-based Beam Line for Clinical Applications," Mar 2019, Imperial College.

[23] L. Beaulieu, M. Goulet, L. Archambault, and S. Beddar, "Current status of scintillation dosimetry for megavoltage beams," *Journal of Physics: Conference Series*, vol. 444, p. 012013, Jun 2013.

[24] C. Le Deroff, A.-M. Frelin-Labalme, and X. Ledoux, "Characterization of a scintillating fibre detector for small animal imaging and irradiation dosimetry," *The British Journal of Radiology*, vol. 90, no. 1069, p. 20160454, 2017. [Online]. Available: https://dx.doi.org/10.1259/bjr.20160454

[25] S. Kellnberger, W. Assmann, S. Lehrack, S. Reinhardt, P. Thirolf, D. Queirós, G. Sergiadis, G. Dollinger, K. Parodi, V. Ntziachristos, and et al., "Ionoacoustic

tomography of the proton bragg peak in combination with ultrasound and optoacoustic imaging," *Scientific Reports*, vol. 6, no. 1, p. 29305, 2016. [Online]. Available: https://dx.doi.org/10.1038/srep29305

[26] K. Parodi and W. Assmann, "Ionoacoustics: A new direct method for range verification," *Modern Physics Letters A*, vol. 30, no. 17, p. 1540025, 2015. [Online]. Available: https://doi.org/10.1142/S0217732315400258

[27] D. Queirós, X. L. Déan-Ben, A. Buehler, D. Razansky, A. Rosenthal, and V. Ntziachristos, "Modeling the shape of cylindrically focused transducers in three-dimensional optoacoustic tomography," *Journal of Biomedical Optics*, vol. 18, no. 7, p. 076014, 2013.

[28] M. Xu and L. V. Wang, "Universal back-projection algorithm for photoacoustic computed tomography," *Physical Review E*, vol. 71, no. 1, 2005.

[29] B. T. Cox, S. R. Arridge, and P. C. Beard, "Photoacoustic tomography with a limited-aperture planar sensor and a reverberant cavity," *Inverse Problems*, vol. 23, no. 6, p. S95–S112, Nov 2007.

[30] B. E. Treeby, E. Z. Zhang, and B. T. Cox, "Photoacoustic tomography in absorbing acoustic media using time reversal," *Inverse Problems*, vol. 26, no. 11, p. 115003, Sep 2010.

[31] J. Zhang, K. Wang, Y. Yang, and M. A. Anastasio, "Simultaneous reconstruction of speed-of-sound and optical absorption properties in photoacoustic tomography via a time-domain iterative algorithm," in *Photons Plus Ultrasound: Imaging and Sensing 2008: The Ninth Conference on Biomedical Thermoacoustics, Optoacoustics, and Acousto-optics*, A. A. Oraevsky and L. V. Wang, Eds., vol. 6856. SPIE, 2008, p. 427–434, backup Publisher: International Society for Optics and Photonics. [Online]. Available: https://doi.org/10.1117/12.764171

[32] P. Burgholzer, G. J. Matt, M. Haltmeier, and G. Paltauf, "Exact and approximative imaging methods for photoacoustic tomography using an arbitrary detection surface," *Physical Review E*, vol. 75, no. 4, 2007.

[33] Y. Xu and L. V. Wang, "Time reversal and its application to tomography with diffracting sources," *Physical Review Letters*, vol. 92, no. 3, 2004.

[34] B. Cox and B. Treeby, "Artifact trapping during time reversal photoacoustic imaging for acoustically heterogeneous media," *IEEE Transactions on Medical Imaging*, vol. 29, no. 2, p. 387–396, 2010.

[35] Y. Hristova, "Time reversal in thermoacoustic tomography—an error estimate," *Inverse Problems*, vol. 25, no. 5, p. 055008, mar 2009. [Online]. Available: https://doi.org/10.48550/arXiv.0812.0606

[36] G. Paltauf, J. A. Viator, S. A. Prahl, and S. L. Jacques, "Iterative reconstruction algorithm for optoacoustic imaging," *The Journal of the Acoustical Society of America*, vol. 112, no. 4, p. 1536–1544, 2002.

[37] I. Orukari, X. Chen, and T. Zhao, "A simulation of ion-acoustic signals after proton flash radiation from a synchrocyclotron," *International Journal of Radiation Oncology*Biology*Physics*, vol. 111, no. 3, p. e133–e134, 2021.

[38] J. Lascaud, P. Dash, H.-P. Wieser, R. Kalunga, M. Würl, W. Assmann, and K. Parodi, "Investigating the accuracy of co-registered ionoacoustic and ultrasound images in pulsed proton beams," *Physics in Medicine amp Biology*, vol. 66, no. 18, p. 185007, Sep 2021.

[39] J. Lascaud, P. Dash, M. Würl, H.-P. Wieser, B. Wollant, R. Kalunga, W. Assmann, D.-A. Clevert, A. Ferrari, P. Sala, and et al., "Enhancement of the ionoacoustic effect through ultrasound and photoacoustic contrast agents," *Scientific Reports*, vol. 11, no. 1, 2021.

[40] S. Kellnberger, W. Assmann, S. Lehrack, S. Reinhardt, P. Thirolf, D. Queirós, G. Sergiadis, G. Dollinger, K. Parodi, V. Ntziachristos, and et al., "Ionoacoustic tomography of the proton bragg peak in combination with ultrasound and optoacoustic imaging," *Scientific Reports*, vol. 6, no. 1, p. 29305, 2016. [Online]. Available: https://dx.doi.org/10.1038/srep29305

[41] H. T. Lau, "Medical applications for particle physics," Ph.D. dissertation, Imperial College London, Feb 2022.

[42] V. Arp, J. M. Persichetti, and G. B. Chen, “The Grueneisen parameter in fluids,” *ASME Journal of Fluids Engineering*, vol. 106, pp. 193–200, Jun. 1984.

[43] F. D. Stacey and J. H. Hodgkinson, “Thermodynamics with the grüneisen parameter: Fundamentals and applications to high pressure physics and geophysics,” *Physics of the Earth and Planetary Interiors*, vol. 286, p. 42–68, 2019.